01 Jan 2014

Phonon Thermal Transport Through Tilt Grain Boundaries in Strontium Titanate

Zexi Zheng

Xiang Chen

Bowen Deng

Aleksandr V. Chernatynskiy
Missouri University of Science and Technology, aleksandrc@mst.edu

et. al. For a complete list of authors, see https://scholarsmine.mst.edu/phys_facwork/483

Recommended Citation

Z. Zheng et al., "Phonon Thermal Transport Through Tilt Grain Boundaries in Strontium Titanate," *Journal of Applied Physics*, vol. 116, no. 7, American Institute of Physics (AIP), Jan 2014.
The definitive version is available at https://doi.org/10.1063/1.4893648

Phonon thermal transport through tilt grain boundaries in strontium titanate

Zexi Zheng,[1] Xiang Chen,[1] Bowen Deng,[2] Aleksandr Chernatynskiy,[2] Shengfeng Yang,[1] Liming Xiong,[1] and Youping Chen[1]
[1]*Department of Mechanical and Aerospace Engineering, University of Florida, Gainesville, Florida 32611, USA*
[2]*Department of Materials Science and Engineering, University of Florida, Gainesville, Florida 32611, USA*

(Received 21 July 2014; accepted 4 August 2014; published online 21 August 2014)

In this work, we perform nonequilibrium molecular dynamics simulations to study phonon scattering at two tilt grain boundaries (GBs) in $SrTiO_3$. Mode-wise energy transmission coefficients are obtained based on phonon wave-packet dynamics simulations. The Kapitza conductance is then quantified using a lattice dynamics approach. The obtained results of the Kapitza conductance of both GBs compare well with those obtained by the direct method, except for the temperature dependence. Contrary to common belief, the results of this work show that the optical modes in $SrTiO_3$ contribute significantly to phonon thermal transport, accounting for over 50% of the Kapitza conductance. To understand the effect of the GB structural disorder on phonon transport, we compare the local phonon density of states of the atoms in the GB region with that in the single crystalline grain region. Our results show that the excess vibrational modes introduced by the structural disorder do not have a significant effect on phonon scattering at the GBs, but the absence of certain modes in the GB region appears to be responsible for phonon reflections at GBs. This work has also demonstrated phonon mode conversion and simultaneous generation of new modes. Some of the new modes have the same frequency as the initial wave packet, while some have the same wave vector but lower frequencies.
 [http://dx.doi.org/10.1063/1.4893648]

I. INTRODUCTION

Strontium titanate ($SrTiO_3$) is a typical perovskite-type ceramic material. It has long been recognized as a potential thermoelectric (TE) material due to its high power factor observed at room temperature. The energy efficiency of TE materials is determined by the dimensionless figure-of-merit $ZT = S^2\sigma T/\kappa$, where S is the Seebeck coefficient, σ the electrical conductivity, k the thermal conductivity, and T the absolute temperature. In the past decades, many efforts have been made to increase the ZT value of $SrTiO_3$ through augmenting the electrical conductivity by doping various elements such as lanthanum, niobium, and yttrium[1] into the two cationic sites.[2] However, the relatively high lattice thermal conductivity is not yet satisfactory.

Recent studies have shown through several feasible ways that the κ value of $SrTiO_3$ can be reduced without adversely affecting the electronic properties of the material. One of the strategies is to introduce nano-grained structures that can give rise to an increased rate of phonon interfacial scattering by the grain boundaries (GBs). Research work on $SrTiO_3$ for this purpose has mainly focused on developing the relationship between the average grain size and the overall thermal conductivity.[2] The underlying mechanisms, however, were unattainable by these research methods. Recent studies also suffered from several other limitations. For example, the Kapitza resistance could not be well inferred from experimental data, because temperature drops also occurred inside the grains. This is probably due to the phonon-defect interaction and/or Umklapp phonon-phonon scattering.[2,3] The mode dependent phonon contribution to heat transfer is unknown, which means the characteristics of phonon transport physics in $SrTiO_3$ is not yet well understood.

The Kapitza resistance or thermal boundary resistance R_κ is a measure of the interface's resistance to heat transfer. If *heat flows across* an *interface*, such as a grain boundary, the interfacial thermal resistance will lead to a temperature discontinuity ΔT at the interface. The heat flux J, the Kapitza resistance R_κ, and the temperature discontinuity ΔT are related by $R_\kappa = \Delta T/J = 1/\sigma_k$, where σ_κ, the inverse of the Kapitza resistance, is called the Kapitza conductance. The GB resistance arises from phonon scattering at the GBs in the medium where phonons are the dominant thermal carriers. It has been suggested that the intensity of scattering depends strongly on the structure of a GB and is highly related to the degree of disorder of the structure and the GB energy.[4,5]

The acoustic mismatch model (AMM) and the diffuse mismatch model (DMM) are two basic theoretical models to predict the interfacial thermal resistance.[6,7] The AMM assumes specular scattering while the DMM assumes diffuse scattering. Both usually fail to give a reasonable approximation of the phonon transmission coefficient in GB thermal transport problems.[4,5] The key conceptual weakness is that neither of them takes the information of the atomic structure into consideration.

The phonon wave-packet dynamics (WPD) method has been developed in order to gain detailed insight into phonon-interface interactions.[11] This method enables us to directly study the mechanism of phonon scattering at the interface. By analyzing the energy transmitted through and reflected back from the boundary, one can determine the transmission coefficient of each phonon mode.

The objective of this work is to study the phonon-GB interactions in $SrTiO_3$ and to quantify the contribution of each phonon mode to the thermal conductance. Two tilt grain boundaries in $SrTiO_3$, the $[001](210)\Sigma5$ GB and the $[001](310)\Sigma5$ GB, are chosen for this study, because the structures of the $[001](210)\Sigma5$ and the $[001](310)\Sigma5$ tilt grain boundaries in $SrTiO_3$ have been identified by scanning transmission electron microscopy (STEM) along with a detailed investigation of their GB energy.[8,9] We employ the WPD method to obtain detailed information on phonon scattering at these GBs. We then calculate the transmission coefficients from the WPD simulations and the other variables through the lattice dynamics (LD) approach to theoretically estimate the Kapitza conductance. For comparison, we also perform molecular dynamics (MD) simulations using the standard nonequilibrium molecular dynamics simulation technique, i.e., the direct method,[10] to measure the Kapitza conductance. The results obtained by the two independent methods will be presented and discussed.

The remaining article is organized as follows. In Sec. II, we describe the two GB structures, the WPD method used in MD simulation to calculate the transmission coefficients, and the LD model used to determine the Kapitza conductance. In Sec. III, we present and discuss the results of this work: (A) the temperature-dependent Kapitza conductance obtained by the WPD method and the LD model, and the comparison of these results with that obtained by the direct method, (B) branch- and frequency-dependent energy transmission coefficients and branch-wise phonon contribution to the overall Kapitza conductance, (C) comparison between the local phonon density of states (PDOS) of atoms in the single crystal grain region and that in the GB region for the two bicrystal systems, and (D) snapshots of wave packets after scattering by the GBs to show mode conversion and excitation of new modes during GB-phonon interactions. Major findings of this work will be summarized in Sec. IV.

II. METHODOLOGY

To construct the computer models of the GBs, the left grain is rotated by an angle α clockwise and then the right grain by the angle α counterclockwise, both about the z axis, in which α is 26.57° for the (210) plane and 18.44° for the (310) plane. A rigid-body translation is then applied on one grain with respect to the other. The applied translational states are $x = 0.0$Å, $y = 0.5$Å, $z = 1.5$Å for the $(210)\Sigma5$ GB and $x = 4.5$Å, $y = 0.5$Å, $z = 0.5$Å for the $(310)\Sigma5$ GB, respectively.[8,9] Thereafter, the structure is further relaxed with a small viscous damping force applied on atoms to drain the kinetic energy. During the relaxation, the system is observed to further adjust itself to a structural state with a minimum GB energy. The side view of the two GB structures is presented in Fig. 1.

In Fig. 2, we present the computer models of the bicrystal $SrTiO_3$ for wave-packet MD simulations and for MD simulations with direct methods, respectively. For the purpose of comparing the predictions based on the two different methods, the same bicrystal systems with periodic boundary conditions (PBC) in all three dimensions are used for both sets of simulations.

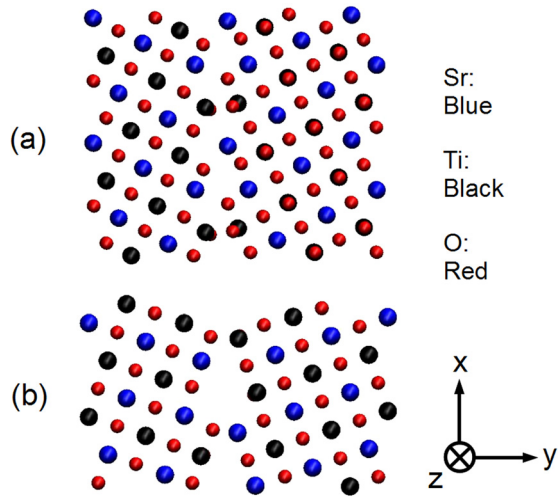

FIG. 1. The GB structure of (a) [001] (210) Σ5 and (b) [001] (310) Σ5. Both of them have reached a very low energy state (well relaxed).

The phonon wave-packet dynamics method is described in Fig. 2(a). The basic idea is to generate a well-defined phonon wave packet in a perfect grain and let it propagate freely towards an interface.[11] When the wave packet encounters the interface (the GB in this work), it is scattered into transmitted and reflected waves. The transmission coefficient t is then determined through E_t/E, where E_t is the transmitted total energy (potential and kinetic energy), and E is the total energy of the original wave packet. The two GB structures are both symmetric about the center of the model. We apply the initial wave packet in Grain A and let it propagate towards Grain B. The propagation direction is indicated by the arrow. A simulation box of about $1500a_0$ in length (half for Grain A and half for Grain B) and $2a_0$ in thickness is employed, where $a_0 = 3.905$Å is the lattice parameter. This length ensures that the simulation box is long enough to simulate long-wavelength wave packets, while the width is chosen to match the smallest repeat unit (SRU) in that direction. We use two SRUs in the $(210)\Sigma5$ GB model, which is $2\sqrt{5}a_0$, and one SRU in the $(310)\Sigma5$ GB model, which is $\sqrt{10}a_0$.

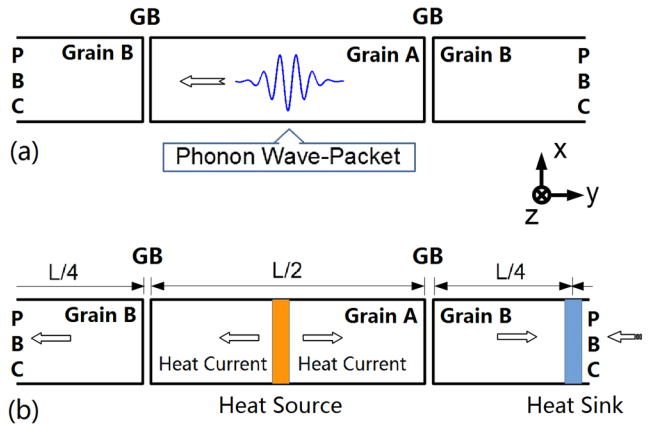

FIG. 2. Schematic illustration of the three dimensional bicrystal simulation systems using (a) the phonon wave-packet method and (b) the direct method.

The phonon wave packets are constructed according to Schelling *et al.*,[11] with atomic displacements given by

$$u_\mu(jl) = A\varepsilon_\mu\left(j\lambda,\vec{k^0}\right)\exp\left[ik_y^0 \times \left(y(jl)-y^0\right) - \frac{\left(y(jl)-y^0\right)^2}{\xi^2}\right], \quad (1)$$

where $u_\mu(jl)$ represents the μth component of displacement u for atom j in the unit cell l; A is the amplitude of the wave and $A = 0.0002a_0$ in this work; $\varepsilon_\mu(j\lambda,\vec{k^0})$ denotes the mode eigenvector of atom j for band λ at a given wave vector $\vec{k^0}$; k_y^0 stands for the y component of $\vec{k^0}$; and ξ^2 controls the spatial extent of the wave packet. The mode eigenvectors can be obtained by solving the dynamical matrix of the perfect crystal. In this work, they are calculated using the analytical lattice dynamics solver in GULP.[12] The initial velocities for each atom are then determined according to

$$\dot{u}_\mu(jl) = \frac{-i}{\sqrt{Nm(j)}}\sum_{\lambda,\vec{k}}\omega\left(\lambda,\vec{k}\right)\varepsilon_\mu\left(j\lambda,\vec{k}\right)\exp\left[ik_y \times y(jl)\right]Q\left(\lambda,\vec{k}\right), \quad (2)$$

where N is the number of unit cells in the crystal; $m(j)$ is the mass of atom j; $\omega(\lambda,\vec{k})$ is the frequency of a particular mode; and $Q(\lambda,\vec{k})$ is the normal mode coordinate given by

$$Q\left(\lambda,\vec{k}\right) = \frac{1}{\sqrt{N}}\sum_{jl}\sqrt{m(j)}\exp\left[-ik_y \times y(jl)\right]\vec{\varepsilon}^*\left(j\lambda,\vec{k}\right)\cdot\vec{u}(jl), \quad (3)$$

in which the asterisk on the mode eigenvector denotes the complex conjugate.

With five atoms in the primitive unit cell, there are fifteen phonon branches in $SrTiO_3$, in which three are acoustic and the remaining twelve are optical. We uniformly sampled more than 12 wave vectors for each acoustic branch on the dispersion curve. This results in a frequency interval less than 0.5 THz. Different from that of acoustic phonons, the dispersion curves of optical phonon are relative flat. The computational cost to simulate the propagation of optical phonon modes is thus very expensive, especially for ionic materials involving Columbic interactions. Therefore, in this work, we only select several representative points in each optical phonon dispersion curve. The modes that have been utilized are those with relatively large group velocities, because these modes are the main contributors to heat conduction.

We calculate the Kapitza conductance according to the well-known lattice dynamics formula[13]

$$\sigma_\kappa(T) = \frac{1}{V}\sum_{\lambda,\vec{k}}^{+}\hbar\omega\left(\lambda,\vec{k}\right)v\left(\lambda,\vec{k}\right)\frac{\partial N_0\left[\omega\left(\lambda,\vec{k}\right),T\right]}{\partial T}t\left(\lambda,\vec{k}\right), \quad (4)$$

where V is the system volume, $\hbar$ the reduced Planck constant, $v(\lambda,\vec{k})$ the group velocity, $N_0[\omega(\lambda,\vec{k}),T]$ the equilibrium Bose-Einstein distribution, and $t(\lambda,\vec{k})$ the transmission coefficient. The summation is over all normal modes inside the first Brillouin zone with polarization λ and wave vector $\vec{k}$. The plus sign means only those modes with positive group velocities are included. It should be pointed out that the allowed number of wave vectors depends on the system size. As we only consider the plane waves incident normal to the GB plane, the number of $\vec{k}$ equals the number of unit cells along the normal direction (y direction). According to Eq. (4), the thermal conductance is a summation over every k points. We would like to note that, however, our WPD simulations cover only a limited number of representative points as described and the rest of modes are taken into account through linear interpolation. Also, the system volume V is not equal to the volume of the simulation cell. Rather, $V = V_{uc} \times N_{\vec{k}}$, with V_{uc} being the volume of the five-atom primitive unit cell and $N_{\vec{k}}$ the number of wave vectors that are included in the summation.

The computer model for MD simulation using the direct method is sketched in Fig. 2(b). Two equal heat currents are formed by adding a certain amount of kinetic energy at the heat source and removing the same amount of energy at the heat sink at each time step. After the system reaches the steady state, we measure the temperature drops across the GBs and determine the Kapitza conductance using $\sigma_k = J/\Delta T$. The generated heat current in this work is about $74\,GW/m^2$.

Both the wave packet dynamics and the direct method MD simulations are performed using the classical MD code LAMMPS.[14] The empirical partially charged Coulombic

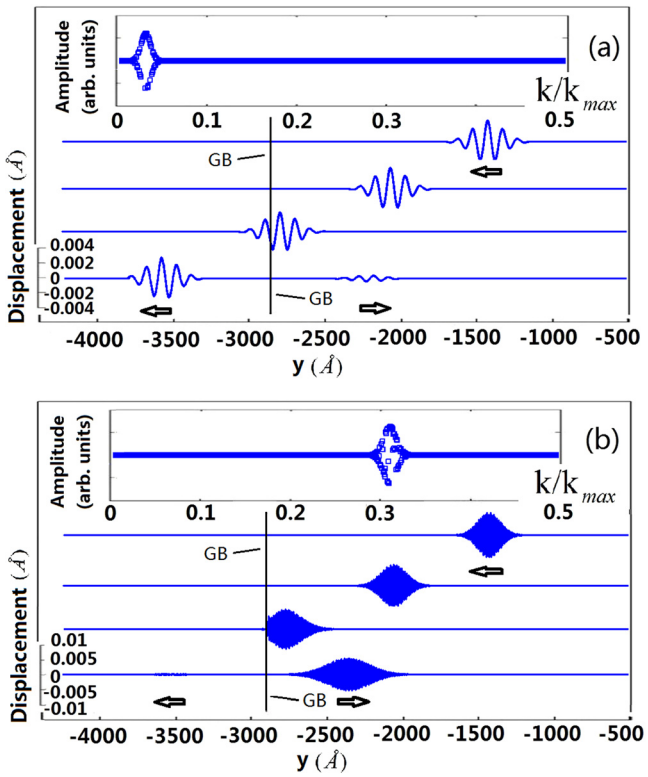

FIG. 3. Snapshots of two TA waves (vibrating in the z direction) propagating and being scattered by the (210) $\sum 5$ GB. In (a), we show a wave packet with $k_y^0 = 0.034k_{max}^{[210]}$ and in (b) a wave packet with $k_y^0 = 0.31k_{max}^{[210]}$, where $k_{max}^{[210]} = \sqrt{5}\pi/a_0$ is the Brillouin zone boundary position. We plot the normal mode coordinate for each wave in the inset.

potential developed by Thomas *et al.*[15] is employed and computed via the Wolf summation method.[16]

III. RESULTS AND DISCUSSION

In Fig. 3, we present snapshots of two TA wave packets propagating and being scattered in the bicrystal system that contains (210)Σ5 GBs. Each wave packet propagates towards the left and meets the GB where it is scattered into a transmitted part that continues moving forward, and a reflected part that moves backward, as indicated by the arrows. The wave packet in Fig. 3(a) has a long wave length, corresponding to a small wave vector of $k_y^0 = 0.034k_{max}^{[210]}$ and a frequency of 0.456 THz, where $k_{max}^{[210]} = \sqrt{5}\pi/a_0$ is the Brillouin zone boundary position for the case of wave vector lying in the [210] direction. The wave packet in Fig. 3(b) has a much shorter wave length, corresponding to a larger wave vector $k_y^0 = 0.31k_{max}^{[210]}$ and a frequency of 3.459 THz. Both wave packets are constructed of TA modes in the same branch with atoms vibrating only along z direction. Their normal mode coordinates in reciprocal space are plotted in the inset of each figure. It is seen from Fig. 3 that the (210)Σ5 GB is almost imperceptible to the TA wave packet with low frequency and long wave length (the first case shown in Fig. 3(a)) but acts like an impenetrable wall to the wave packet with higher frequency and very short wavelength (the second case shown in Fig. 3(b)). Similar frequency- or wavelength-dependent phonon-GB interaction is also found in the simulations with waves in the other two acoustic branches as well as with the (310) Σ5 GB. These results are hence not plotted.

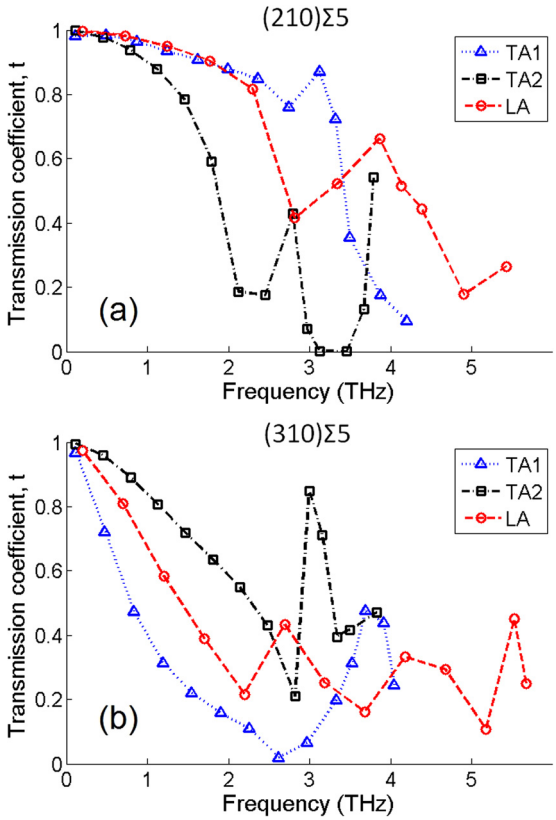

FIG. 4. Frequency-dependent energy transmission coefficients of the three acoustic branches. In (a), we present the results of (210) Σ5 GB and in (b) the results of (310) Σ5 GB.

A. Transmission coefficient and Kapitza conductance

In Fig. 4, we present the frequency-dependent energy transmission coefficients of acoustic phonons across the two GBs, in which $t = 1$ means that all the energy is transmitted, while $t = 0$ means all the energy is reflected back. The actual values measured in this work are between the two limits. As we can see from Fig. 4(a), the wave packet in Fig. 3(a) with the most of the waves being transmitted through the (210) GB has a very high transmission coefficient value of 0.98 (the 2nd point in the curve labeled as TA2). By contrast, the wave packet in Fig. 3(b) with most of the waves being reflected has a very low transmission coefficient value of 0.001 (the 12th point in the curve labeled as TA2) in Fig. 4(a).

The overall trend for the acoustic phonons is that the transmission coefficient decreases monotonically with increasing frequency (decreasing wavelength) when the frequency is low and the wavelength is large, and it decreases more sharply for (310) Σ5 GB than for (210) Σ5 GB. However, when the frequency reaches about 3 THz, the transmission coefficient does not decrease with increasing frequency. It fluctuates instead, suggesting the phonon-GB interaction then becomes more complicated when the corresponding wavelengths have decreased to the length scale that is comparable to the GB thickness.

It can be observed in Figs. 4(a) and 4(b) that the (210) GB generally has higher transmission coefficients than the (310) GB. This suggests that GBs with higher density and lower energy have higher transmission coefficients. It should be noted that, however, the effect of phonon-GB interaction on the transmission coefficients is branch-dependent. The transmission coefficients of the TA1 branch (modes vibrating along x direction) across the (210) GB are the highest among the three branches, while that across the (310) GB are the lowest.

In Fig. 5, we plot the frequency-dependent energy transmission coefficients of the selective optical modes. It is seen from Fig. 5 that the transmission coefficients of optical modes are generally low. They are randomly distributed between 0 and 0.5. No obvious relationship between phonon transmission coefficients and phonon frequency can be identified.

In Fig. 6, we compare the temperature dependence of the Kapitza conductance measured by using the direct method and that by the WPD together with the LD formula expressed in Eq. (4). The values of the Kapitza conductance of the two GBs at temperature T = 500 K obtained by using the two methods are summarized in Table I.

It is seen from Fig. 6 and Table I that the results of the GB thermal conductance obtained by the direct method are in reasonably good agreement with those obtained from the LD theoretical prediction using Eq. (4) with the transmission coefficients obtained by the WPD simulations, i.e., the WPD + LD method. In addition, both methods predict that the Kapitza conductance increases with increasing

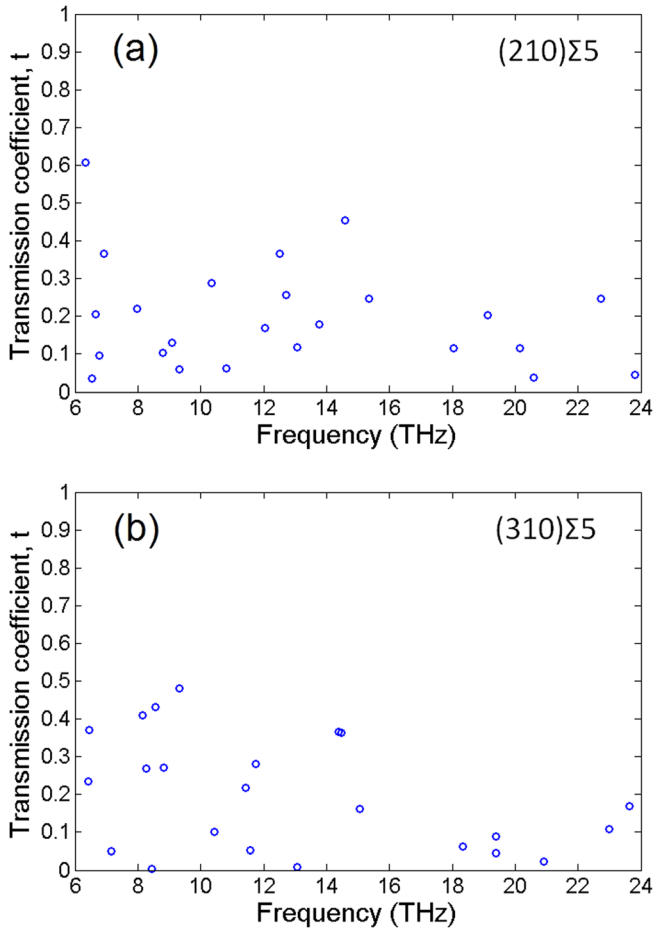

FIG. 5. Energy transmission coefficients of selective optical modes vs. frequency. In (a), we present the results of (210) Σ5 GB and in (b) the results of (310)Σ5 GB.

temperature. Also, both methods predict that the (210) Σ5 GB always has a higher Kapitza conductance than the (310) Σ5 GB for temperature ranging from 200 K to 1000 K. However, the Kapitza conductance of both GBs predicated by the direct method exhibits a linear dependence on temperature, while that by the WPD + LD shows a much weaker dependence on temperature, especially at high temperature.

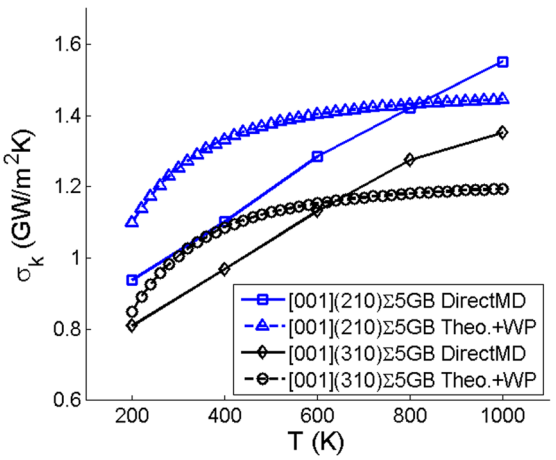

FIG. 6. Temperature dependence of the Kapitza conductance measured through direct MD method and calculated theoretically using Eq. (4) with transmission coefficients determined from wave packet method.

TABLE I. Kapitza conductance (GW/m^2K) measured at 500 K.

Method	(210) Σ5 GB	(310) Σ5 GB
Direct Method	1.19	1.05
WPD + LD	1.38	1.13

This discrepancy is not unexpected since the only temperature dependent term we have in Eq. (4) is the phonon number, N_0, while the anharmonic effects arising from finite temperature may change phonon properties such as the phonon dispersion relation from which the frequency and the group velocity are estimated. Another reason for the difference is that the WPD + LD method uses quantum occupation numbers N_0, while the direct method is fully classical; thus the temperature dependence captured by the WPD + LD is due to the quantum effects, while in direct method it is due to anharmonicity.

B. Phonon contribution to the GB thermal conductance

The mode-wise phonon contributions to the GB thermal conductance are calculated using Eq. (4). Summing over the contributions from all the modes in each branch leads to the phonon contribution to the overall Kapitza conductance from each branch. We plot in Fig. 7 the branch-wise contribution at T = 600 K. Here, branches 1–3 are, respectively, the TA1 (vibration in x), the TA2 (vibration in z), and the LA acoustic phonons. Branches 4–15 are the optical phonons, in which branches 4, 8, 10, 14 are the TO phonons and the rest

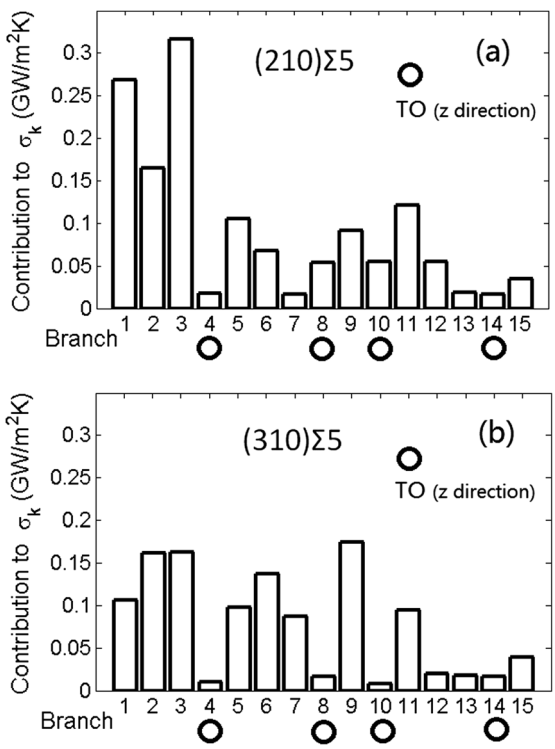

FIG. 7. Branch-wise phonon contribution to the overall Kapitza conductance at T = 600 K. In (a), we show the results for (210) Σ5 GB and in (b) the results for (310) Σ5 GB. The branches marked with circles are the TO modes with atoms vibrating in z direction.

are the hybrid of TO and LO modes in x and y directions. It is seen from Fig. 7 that the optical phonons (branch 4–15) have a significant contribution to the overall thermal conductance, accounting for over 50% of the energy transport across the (210) Σ5 GB and over 60% across the (310) Σ5 GB.

Because of the 2D nature of the bicrystal systems employed in this work, the atomic vibrations in the x and y directions are coupled. Our results show that the phonon modes in these two directions, especially the high-frequency optical modes, are the major contributors to the GB thermal conductance. By contrast, the contributions of the phonon modes in which atoms vibrate in the z direction, i.e., the out-of plane TO modes (marked with circles in Fig. 7), to the GB thermal conductance are insignificant.

In Fig. 8, we present the phonon cumulative contribution to the Kapitza conductance. It is seen from Fig. 8 that for the bicrystal system that contains the (210) GB, phonon modes with low frequencies <4 THz account for about 50% of the overall Kapitza conductance. However, for the system with the (310) GB, the contributions from medium to high frequency modes are as significant as that from the low frequency modes. This is evidenced by the approximately linear dependence of the cumulative contribution on frequency for frequencies up to ~15 THz.

C. Examination of phonon density of states

We calculate the phonon density of states according to Eq. (5), which is basically the Fourier transform of the mass-weighted velocity autocorrelation function.[17,18]

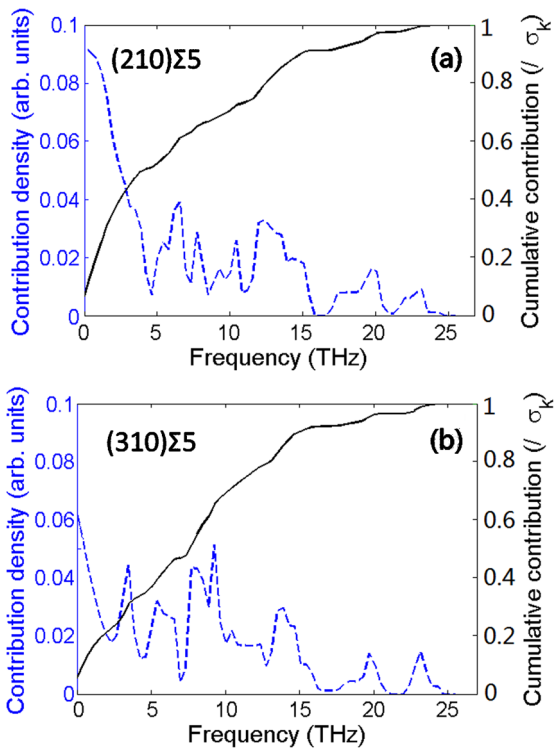

FIG. 8. Phonon cumulative contribution to the Kapitza conductance along with the contribution density as a function of frequency. In (a), we present the results for (210) Σ5 GB and in (b) for (310) Σ5 GB.

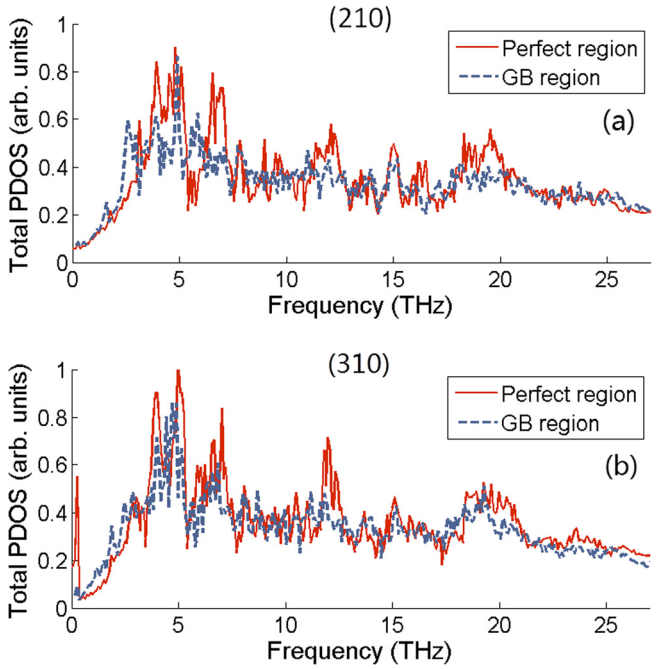

FIG. 9. Total phonon density of states of the bicrystal system with (a) (210) Σ5 GB and (b) (310) Σ5 GB. The red solid line depicts the PDOS of the perfect region and the gray dashed line depicts the PDOS of the GB region.

$$D(\omega) = \frac{1}{k_b T}\int e^{-i\omega t}\sum_j m(j)\langle \vec{u}(jl,t)\cdot\vec{\ddot{u}}(jl,0)\rangle dt, \quad (5)$$

where k_b is the Boltzmann constant and T the system temperature. The angle brackets denote an average over all starting times for the velocity product of each atom and also over all unit cells.

In Fig. 9, we present the comparison between PDOS for atoms in the GB region (the dashed gray line) and that in the perfect single crystalline grain region (the solid red line). In this work, we choose the GB region to be within 6 Å from the center of the GB plane on both sides. A mismatch between the PDOS for atoms in the disordered GB region and that in the perfect crystalline grain region can be clearly observed.

PDOS is primarily a function of the local atomic structure. To understand the effect of the GB structural disorder on the frequency- and branch-dependent energy transmission coefficients presented in Fig. 4, we plot in Figs. 10(a) and 10(b) the local PDOS calculated from the velocity correlations parallel to the (210) GB (x direction) and that perpendicular to the (210) GB (y direction), respectively. For the long simulation cell with small cross-sectional area employed in this work, it can be seen from the phonon dispersion relations that these local PDOS mainly reflect the density of states of the TA1 phonons (vibrating in x direction, Fig. 10(a)) and that of the LA phonons (vibrating in y direction, Fig. 10(b)), respectively.

The mismatch between the local PDOS curves indicates a difference between the numbers of phonon modes present in the two regions. In Fig. 10(a), we observe that in the frequency region from about 3.5 to 4.4 THz, the local PDOS curve for the grain region is much higher than that for the

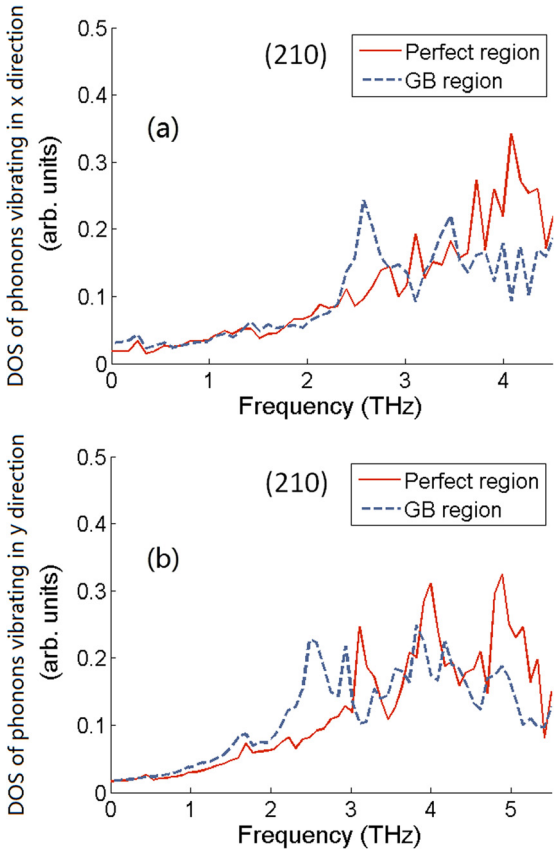

FIG. 10. Local PDOS calculated from velocity correlations (a) parallel to the GB (x direction) and (b) perpendicular to the GB (y direction) in the bicrystal system with (210) Σ5 GB. The red solid line is the PDOS of the perfect region and the gray dashed line the PDOS of the GB region. Only partial frequency bands are shown.

(210) GB region. This implies that many phonon modes with these frequencies are not allowed in the (210) GB region and hence are unable to propagate from the grain region into the GB region. As a result, in Fig. 4(a), we observe an abrupt drop in the transmission coefficients of the TA1 phonons occurred at about 4 THz. Similarly, the occurrence of the lowest transmission coefficient of the LA phonons at about 5 THz shown in Fig. 4(a) is also in correspondence with the mismatch between local PDOS curves observed in Fig. 10(b) for the same frequency range.

There are two kinds of mismatches between the local PDOS curves. When the number of phonon modes in the grain region is more than that in the GB region, some phonon modes cannot propagate into the GB region, resulting in a low energy transmission. On the other hand, when the number of phonon modes in the grain region is less than that in the GB region, for example, the TA1 and the LA modes at frequencies ∼2.5 THz, the transmission coefficients are found to be higher than 0.7. Thus, this kind of mismatch does not have a significant effect on phonon transmission. Our simulation results confirm a previous observation that the atomic–scale structural disorder at GBs results in additional vibrational modes.[19] However, the results of this work show that the excess vibrational modes do not have a strong effect on phonon transmission.

In Fig. 11, we present the local PDOS calculated from velocity correlations parallel to the (210) GB (z direction).

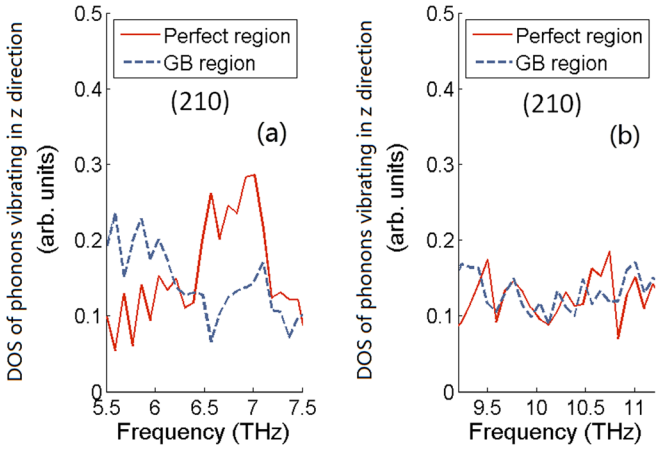

FIG. 11. PDOS calculated from velocity correlations parallel to the GB (z direction) in the bicrystal system with (210) Σ5 GB. The red solid line depicts the PDOS of the perfect region and the gray dashed line depicts the PDOS of the GB region. Only partial frequency bands are shown.

According to the phonon dispersion relations, for the frequency ranges plotted, they can be identified as mainly of the TO phonons in branch 4 and branch 8, respectively. The effect of local PDOS mismatch on the transmission coefficients is again demonstrated. It is seen from Fig. 11(a) that there is a significant mismatch between the PDOS for the atoms in the grain region and that in the GB region. As a consequence, the contribution of the TO phonon branch 4 to the thermal conductance is very small, as shown in Fig. 7(a). On the other hand, the mismatch in Fig. 11(b) is less significant than that in Fig. 11(a), and the contribution of the TO phonon branch 8 to the thermal conductance is much larger.

D. Mode conversion and excitation

In Fig. 12, we present snapshots of the displacements of a LA wave packet (vibrating along y direction with

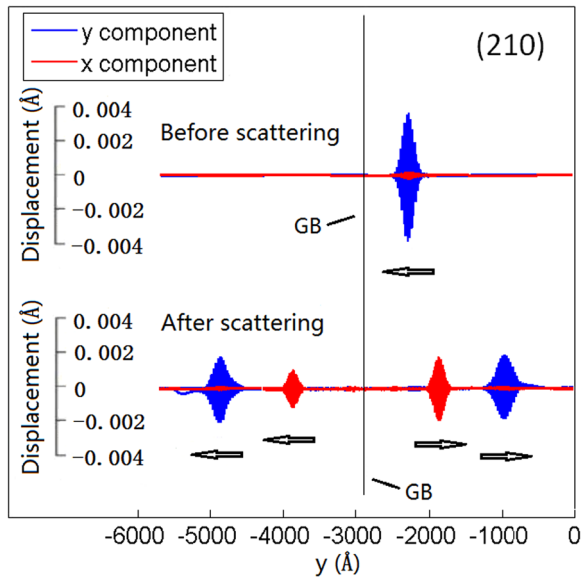

FIG. 12. A LA wave packet (vibrating along y direction, in blue) with initial wave vector $k_y^0 = 0.127k_{max}^{[210]}$ and frequency of 2.82 THz is scattered by the (210) Σ5 GB. After scattering, a new mode in the TA branch (vibrating along x direction, in red) with same frequency is excited.

frequency of 2.82 THz) before and after scattering. A new TA mode is observed after the scattering. The new TA mode has the same frequency as the initial LA mode, implying that the scattering is elastic. It should be noted that simulation results show that at high frequency the polarizations or the eigenvectors of LA and TA phonons are highly coupled. This coupling facilitates phonon mode conversion.

In Fig. 13, we plot snapshots of the displacements of a TO wave packet after scattering. It is seen from Fig. 13 that, after scattering, two new modes that have the same frequency are excited. Note that the furthest left and the furthest right wave packets each contains two different modes; these two modes (mode1 and mode 2) although with different phonon wave vectors in the same phonon branch, they have the same frequency as well as the same group velocity, with one of them from the other half of the first Brillouin zone, and hence they can travel together as one wave packet.

Figure 14(a) presents the snapshot of displacements of an optical wave packet with initial wave vector $k_y^0 = 0.238k_{max}^{[310]}$ and frequency 11.43 THz after scattering. From Fig. 14(a), we see that the wave packet is scattered into several transmitted and reflected waves. It should be noted that, after scattering, each of the waves plotted in Fig. 14(a) actually contains several different phonon modes.

In Fig. 14(b), we identify all the modes excited after the scattering using modal analysis of the displacements shown in Fig. 14(a) through inverse Fourier transform and plot them together with the dispersion curves of the corresponding branches. Note that the original wave packet is a hybridized modes of LO and TO. The phonons wave modes after scattering are also hybridized modes, involving both x and y direction vibrations. It can be seen from Fig. 14(b) that the initial wave packet in the high-frequency optical branch (the branch 9) is scattered into a series of waves that have the same or lower frequencies. These newly generated waves either have the same frequency or the same wave vector as the initial wave. For waves that have same wave vectors, their frequencies are lower than that of the initial waves,

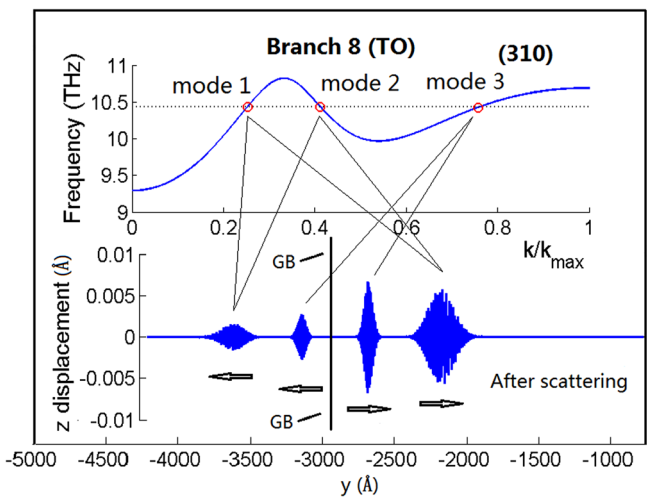

FIG. 13. A TO wave packet (from branch 8, vibrating along z direction, the out of plane direction) of mode 1 ($k_y^0 = 0.253k_{max}^{[310]}$, frequency 10.44 THz) is scattered by the (310) Σ5 GB. In the inset is the dispersion curve of branch 8. The Brillouin zone boundary position $k_{max}^{[310]} = \sqrt{10}\pi/a_0$.

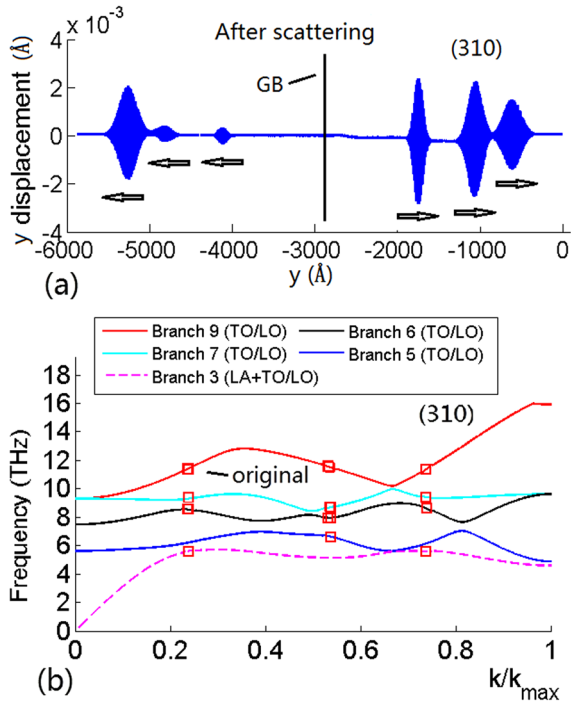

FIG. 14. A wave packet with initial wave vector $k_y^0 = 0.238k_{max}^{[310]}$ and frequency 11.43 THz from the optical phonon branch 9 (vibrating along x and y directions) is scattered into multiple waves by the (310) Σ5 GB.

indicating that lower frequency or lower energy phonon modes can be generated from GB scattering of high-frequency high-energy phonons.

IV. CONCLUSIONS

In this work, we have performed MD simulations using the wave-packet dynamics method to study phonon-GB interactions at two different tilt grain boundaries in $SrTiO_3$. The frequency-dependent energy transmission coefficients are calculated and the contributions of different phonon modes and branches to the GB thermal conductance are quantified. The simulation results show that neither AMM (which predicts the transmission coefficient, t, to be 1 for GB interface) nor DMM (which predicts t to be 0.5 for GB scattering) can predict the transmission coefficients for the two GBs in $SrTiO_3$.

Since no experimental measurements of Kapitza resistance for the two GBs have been reported, MD simulations using the direct method are also performed to directly measure the GB thermal conductance. The results of the overall GB thermal conductance obtained by the two independent methods are found to agree reasonably well, except for the temperature dependence. The discrepancy in the temperature effect predicted by the two methods is not unexpected since the wave packet dynamics method is essentially a zero-temperature method and the temperature dependence in the theoretical equation is due to quantum effects, while in the direct method it is due to anharmonicity.

Despite these limitations, the wave packet dynamics method combined with the theoretical equation of lattice dynamics has unique advantages over the direct method in providing detailed information to understand the mechanisms

underlying the phonon-GB scattering, estimating the scattering rate for phonons with different modes, and quantifying the contribution from phonons of different branches or within a certain frequency range to the overall Kapitza conductance.

Many theoretical models of phonon thermal transport ignore the effects of optical phonons due to their small group velocity. Since simulation of optical phonon propagation is extremely expensive, all existing simulation works on phonon transport properties either ignore the contribution of optical branches[20–22] or assume a uniform thermal transmission coefficient for all of the optical branches based on a few simulations of longitudinal optical modes.[4,23] Contrary to common belief, our results show that the optical modes in $SrTiO_3$ contribute significantly to thermal transport properties, accounting for more than 50% of the overall GB conductance for the two GB structures studied in this work. Nevertheless, it should be noted that the contributions from the out-of plane TO modes to the GB thermal conductance are insignificant.

The mismatch between the local PDOS of atoms in the single crystalline grain region and that in the GB region indicates a difference between the numbers of phonon modes allowed or present. The results of this work confirm that the structural disorder at GBs introduces additional vibrational modes. The excess vibrational modes caused by the structural disorder, however, do not have a strong effect on phonon transmission across the GBs when the number of phonon modes in the GB region is higher than that in the grain region. By contrast, when the number of phonon modes in the grain region is more than that in the GB region, a low energy transmission results, implying that some phonon modes cannot transmit across the GB as a consequence of the mismatch. Thus, the local PDOS may be used to provide information about what structures or defects scatter specific phonons.

Through visualization of phonon scattering at the GBs, we have demonstrated mode conversion and simultaneous generation of new modes that either have the same frequency as the initial wave packet or that have the same wave vector, but lower frequency. It is found that lower frequency or lower energy phonon modes can be generated from scattering of high-frequency high-energy phonons.

ACKNOWLEDGMENTS

This material is based on the work supported by the grant DOE/DE-SC0006539 funded by the U.S. Department of Energy, Office of Science. S.Y. and X.C. were also supported in part by National Science Foundation under Award Nos. CMMI-1233113 and CMMI-1129976. A.C. acknowledges support from Idaho National Laboratory, LDRD #13-105. The work of B.D. was supported as a subcontractor of the U.S. Government under DOE Contract No. DE-AC07-05ID14517, under the Energy Frontier Research Center (Office of Science, Office of Basic Energy Science, FWP 1356). Accordingly, the U.S. Government retains and the publisher (by accepting the article for publication) acknowledges that the U.S. Government retains a nonexclusive, paid-up, irrevocable, world-wide license to publish or reproduce the published form of this manuscript, or allow others to do so, for U.S. Government purposes.

[1]C. Yu, M. L. Scullin, M. Huijben, R. Ramesh, and A. Majumdar, Appl. Phys. Lett. **92**, 092118 (2008).
[2]B. M. Foley, H. J. Brown-Shaklee, J. C. Duda, R. Cheaito, B. J. Gibbons, D. Medlin, J. F. Ihlefeld, and P. E. Hopkins, Appl. Phys. Lett. **101**, 231908 (2012).
[3]Y. Wang, K. Fujinami, R. Zhang, C. Wan, N. Wang, Y. Ba, and K. Koumoto, Appl. Phys. Express **3**, 031101 (2010).
[4]S. Aubry, C. J. Kimmer, A. Skye, and P. K. Schelling, Phys. Rev. B **78**, 064112 (2008).
[5]P. K. Schelling, S. R. Phillpot, and P. Keblinski, J. Appl. Phys. **95**, 6082 (2004).
[6]E. T. Swartz and R. O. Pohl, Rev. Mod. Phys. **61**, 605 (1989).
[7]W. A. Little, Can. J. Phys. **37**, 334 (1959).
[8]M. Imaeda, T. Mizoguchi, Y. Sato, H. S. Lee, S. D. Findlay, N. Shibata, T. Yamamoto, and Y. Ikuhara, Phys. Rev. B **78**, 245320 (2008).
[9]H. S. Lee, T. Mizoguchi, J. Mitsui, T. Yamamoto, S. J. L. Kang, and Y. Ikuhara, Phys. Rev. B **83**, 104110 (2011).
[10]P. K. Schelling, S. R. Phillpot, and P. Keblinski, Phys. Rev. B **65**, 144306 (2002).
[11]P. K. Schelling, S. R. Phillpot, and P. Keblinski, Appl. Phys. Lett. **80**, 2484 (2002).
[12]J. D. Gale, JCS Faraday Trans. **93**, 629 (1997). The software is freely available from https://www.ivec.org/gulp/.
[13]D. A. Young and H. J. Maris, Phys. Rev. B **40**, 3685 (1989).
[14]S. J. Plimpton, J. Comput. Phys. **117**, 1 (1995).
[15]B. S. Thomas, N. A. Marks, and B. D. Begg, Nucl. Instrum. Methods Phys. Res. B **228**, 288 (2005).
[16]D. Wolf, P. Keblinski, S. R. Phillpot, and J. Eggebrecht, J. Chem. Phys. **110**, 8254 (1999).
[17]M. T. Dove, *Introduction to Lattice Dynamics* (Cambridge University Press, Cambridge, 1993).
[18]J. Lukes and H. Zhong, J. Heat Transfer **129**, 705 (2007).
[19]S. Stankov, Y. Z. Yue, M. Miglierini, B. Sepiol, I. Sergueev, A. I. Chumakov, L. Hu, P. Svec, and R. Rüffer, Phys. Rev. Lett. **100**, 235503 (2008).
[20]A. Ward and D. A. Broido, Phys. Rev. B **81**, 085205 (2010).
[21]A. Ward, D. A. Broido, D. A. Stewart, and G. Deinzer, Phys. Rev. B **80**, 125203 (2009).
[22]D. A. Broido, M. Malorny, G. Birner, and D. A. Stewart, Appl. Phys. Lett. **91**, 231922 (2007).
[23]C. Kimmer, S. Aubry, A. Skye, and P. K. Schelling, Phys. Rev. B **75**, 144105 (2007).